



Article

Laser Melt Infiltration of UHMWPE into the Binary Coatings of Strontium Apatite and Colloidal Silica

Akira Furukawa *  and Yasuhito Tanaka 

Department of Orthopedic Surgery, Nara Medical University, 840 Shijo-cho, Kashihara 634-8521, Nara, Japan

* Correspondence: furukawa_akira@naramed-u.ac.jp; Tel.: +81-744-29-8873

Abstract: Medical-grade ultrahigh molecular weight polyethylene (UHMWPE) is the material of choice for sliding surfaces in various articular joint implants owing to its excellent biocompatibility and superior physical properties, such as an exceptionally low coefficient of friction and excellent durability. However, the bioinert nature of UHMWPE limits its extended use in rapidly advancing medical fronts. In this study, bioactive surface modifications of UHMWPE were addressed using a newly developed laser-melt infiltration technique. UHMWPE was coated with binary mixtures of strontium apatite and colloidal silica particles and irradiated using a 30 W CO₂ laser to reach the maximum temperature of 150 ± 5 °C. UHMWPE melts infiltrated the porous matrices of the coatings by capillary force and formed surface-selective composite materials between them. Capillary rise heights were evaluated by observing the uplift of the substrate after the selective dissolution of the coating substances and were found to be much higher than the estimated values based on the Lucas–Washburn equation. This finding suggests that the melt viscosity of UHMWPE confined within the nanopores might be significantly lower than that measured at macroscopic scales. Both strontium and silicate ions are known osteo-inductive factors, and their concentrations eluted from the binary coatings were substantially higher than those found in the single coatings.

Keywords: apatite; colloidal silica; melt infiltration; UHMWPE; binary coatings



Citation: Furukawa, A.; Tanaka, Y. Laser Melt Infiltration of UHMWPE into the Binary Coatings of Strontium Apatite and Colloidal Silica. *Coatings* **2023**, *13*, 580. <https://doi.org/10.3390/coatings13030580>

Academic Editor: Catalina Natalia Cheaburu-Yilmaz

Received: 10 February 2023

Revised: 27 February 2023

Accepted: 1 March 2023

Published: 7 March 2023



Copyright: © 2023 by the authors. Licensee MDPI, Basel, Switzerland. This article is an open access article distributed under the terms and conditions of the Creative Commons Attribution (CC BY) license (<https://creativecommons.org/licenses/by/4.0/>).

1. Introduction

Among the various materials available for orthopedic applications, ultrahigh molecular weight polyethylene (UHMWPE) remains in the unique position of the chosen material for sliding components in various articular implants owing to its characteristic low coefficient of friction, biocompatibility, chemical resistance, physical durability, and superior mechanical properties [1,2]. However, there are still various problems associated with the difficulties in surface modification and bio-inertness of UHMWPE for extended usage in current and continually evolving medical fields. For instance, in anatomic total shoulder arthroplasty (TSA), UHMWPE is used in the glenoid component of the implant for TSA; the insufficient fixation of the glenoid is one of the main factors for implant loosening, frequently causing postoperative pain in patients and ultimately leading to implant failure [3,4]. The glenoid component is usually fixed to the glenoid cavity of the scapula, either with the aid of bone cement or directly fixed via the press-in method. UHMWPE itself cannot bind adhesively to bone or bone cement, and some aids for improved adhesion are indispensable for the successful implantation and long-term survival of the implant. In recent decades, several studies have focused on making adhesive modifications to innate UHMWPE. Poulsson et al. [5] treated UHMWPE substrates with UV irradiation under an ozone atmosphere and introduced active carboxyl groups on the surface. The modified UHMWPE substrates exhibited excellent cell attachment and enhanced the proliferation of human primary osteoblast-like cells. Various types of plasma treatments are also among the frequently applied methods for improving the wettability of different polymers, such as using atmospheric plasma treatments on UHMWPE. Significant improvements in its

bioactivity and enhanced adhesive strength to bone cements have been demonstrated [6,7]. More et al. [8] investigated the effects of UHMWPE surface modification on cellular adhesion using electron cyclotron resonance plasma treatment and showed that the duration of plasma treatment governs whether the polymer surface supports either osteoblast or osteoclast differentiation. Titanium coatings on UHMWPE substrates have been attempted using the ionic plasma deposition technique [9], with increased osteoblast proliferation and calcium deposition from the cell culture medium clearly demonstrated.

Applications of high-power lasers for the improvement of bioactivities on various polymer substrates were intensively investigated [10–12]. Laser irradiation on the polymer surface can induce both chemical and physical changes to the irradiated surface according to its energy density (J/m^2) at the laser spot. These changes can modulate cell–polymer interactions through various effects, including (1) chemical interactions between newly introduced functional groups and adherence-promoting proteins [13,14]; (2) the mechanical stimulation of topographical patternings to the integrin-mediated focal adhesion [15], and (3) other effects such as the laser-induced residual stress (IRS) effect which stimulates cell migration and alignment [16].

For instance, polyethylene terephthalate (PET) film was irradiated by CO₂ pulsed laser at the wavelength of 9.25 μm and KrF excimer laser at 248 nm with various number of pulses [17]. Cell adhesion and its spreading properties were investigated using fibroblast cells on the laser-treated surfaces and significant improvements in cell attachment and proliferation were confirmed in comparison with the unmodified PET. Similarly, poly(ether-ether-ketone; PEEK) was irradiated by a femtosecond laser and as the results of low-temperature plasma etching, active sites including amorphous carbon and carbon-hydroxyl were formed on the PEEK surface. Through the cell culture experiments on the treated surface, increased cell proliferation was confirmed [18].

As for UHMWPE, except for some examples of laser abrasion study conducted by a 438 nm high-energy pulsed laser [19], and other various studies on the selective laser sintering process (SLS) to fabricate the 3D constructs from powdered UHMWPE using commercial high-power CO₂ lasers [20,21], direct laser treatments for surface modification seems to be inadequate for UHMWPE, because of its inefficient absorption capacity for the incident photon energy due to the lack of appropriate functional groups in the polymer chains. In order to increase its nominal absorption coefficient, UHMWPE substrates were coated with carbon [22] and irradiated by lasers at the wavelengths of 1064, 532, and 355 nm, respectively. Influences of processing conditions on wettability and roughness, which affect cell adhesion properties, were quantitatively evaluated.

Another important method for the surface modification of UHMWPE is the formation of composite materials with various fillers, including hydroxyapatite [23,24], aluminum oxide [25], titanium oxide [26], carbon nanotubes, and graphene [27], which has been intensively investigated by various researchers; however, intrinsic difficulties in homogeneously blending these fillers within the UHMWPE matrix still exist.

Despite the substantial improvements in UHMWPE biocompatibility, direct bonding between UHMWPE and hard tissue *in vivo* has not yet been established; most of the bearing materials of the implants for total joint arthroplasty use UHMWPE components in combination with titanium endplates to fix them to the hard tissue in the body. However, the direct bonding between hard tissue and titanium plates with a high Young's modulus is a potential risk factor for bone resorption owing to the stress shielding effect [28]. Therefore, applying osseointegral properties to the UHMWPE surface would be significantly beneficial for establishing the much more simplified and reliable designs of various articular implants and would contribute to their long-term stability. Recently, a versatile method for integrating apatite coatings with poly(ether ether ketone, PEEK) using a CO₂ laser was successfully established [29], in which the melts of PEEK infiltrated the porous matrices of apatite coatings by capillary force, realizing the surface-selective formation of the PEEK-apatite composites. In this study, we applied this laser-induced melt infiltration

technique to the surface modification of UHMWPE with apatite and colloidal silica coatings to fabricate a new type of bioactive UHMWPE.

Sr ions are known to promote bone formation and suppress bone resorption. In previous studies, a simple method to synthesize a series of substituted strontium apatites was established [30]. These strontium apatites were coated onto various substrates to demonstrate notably enhanced bone formation on the surface of the substrates, including artificial ligaments [31], bone graft substitutes [32], and PEEK material for spinal implants [33]. In these studies, we demonstrated that strontium ions are steadily released from the coatings, with their concentrations controlled by the amount of apatite coating [32].

Silicate ions are also known to stimulate bone growth by enhancing osteoblast activity while inhibiting osteoclasts [34]. Several studies have been conducted on preparing and characterizing hydroxyapatite–silica composites to establish superior biocompatible scaffolds in tissue engineering [35–37], and various coating applications of hydroxyapatite–silica composites using deposition techniques have also been reported [38,39].

In this study, we focused on binary mixtures of strontium apatite and colloidal silica and coated them on a UHMWPE substrate using the melt infiltration technique. The dissolution behaviors of these binary coatings were studied by quantitatively analyzing the eluting ions from the coatings using inductively coupled plasma atomic emission spectroscopy (ICP-AES).

2. Materials and Methods

2.1. Preparation and Characterization of Strontium Apatites

All the chemicals were purchased from Fujifilm Wako Chemicals (Osaka, Japan). Colloidal silica dispersed in methanol (ORGANOSILICASOL[®], MA-ST, solid content: 30 wt.%, particle size: 12 nm) was supplied by Nissan Chemical Corporation, Tokyo, Japan. HBSS(+) without phenol red (Code No. 084-08965: Fujifilm Wako Chemicals, Osaka, Japan) was used for a simulated body fluid (SBF) in this study.

The preparation and characterization of zinc and silicate co-substituted strontium apatite (SrZnSiP) were described in a previous study [17], briefly explained as follows: silicate-substituted strontium apatite was prepared via alkaline hydrolysis of α -strontium hydrogen phosphate (α -SrHPO₄) with sodium metasilicate; the resultant product was treated with zinc chloride in ammoniacal media to obtain the desired product, SrZnSiP.

2.2. Preparation of Coating Solutions

SrZnSiP was dispersed in ethanol using the following procedure: 25 g of ethanol and 5 g of SrZnSiP powder were mixed with 0.3 g of citric acid monohydrate (2-hydroxy-1,2,3-propanetricarboxylic acid monohydrate, C₆H₈O₇·H₂O) and 100 g of yttria-stabilized zirconia (Y₂O₃-ZrO₂) balls (0.3 mm diameter (YTZ[®]-0.3), Nikkato Co., Ltd., Osaka, Japan). The mixture was added to a 100 mL plastic bottle, placed on a shaking apparatus (Laboratory Shaker MK201D, Yamato Scientific Co., Ltd., Tokyo, Japan), and shaken horizontally at 200 c/m for 24 h; the resulting dispersion was separated through decantation. The solid concentration of the dispersion was measured via ethanol evaporation and thereafter adjusted to 5 wt.% using ethanol.

A colloidal silica coating solution was prepared by adding 0.15 g of citric acid monohydrate (10 g) to Organosilicasol, MA-ST solution (30 wt.%), and the solid concentration of colloidal silica was adjusted to 5 wt.% using ethanol. Solutions of strontium apatite and colloidal silica were prepared by mixing each solution with the appropriate ratios, with the total concentration adjusted to 5 wt.% using ethanol.

2.3. Coatings on UHMWPE Disks and Laser Bonding by CO₂ Laser Irradiation

UHMWPE sheets were purchased from Yodogawa Hu-Tech Co., Ltd., Osaka, Japan, and processed using an appropriate punch-cutting die to manufacture identical disks with diameters and thicknesses of 13 mm and 2 mm, respectively. Before coating, the UHMWPE disks were immersed in acetone for 24 h, rinsed with ethanol, and dried at 70 °C in

an oven. Each UHMWPE disk was coated with 20 μL of coating solution and air-dried. The calculated coating weight was 1.0 mg on a 1.33 cm^2 area. The coated UHMWPE disk was placed under a CO_2 laser (3-Axis Laser Marker ML-Z9510, Keyence Corp., Osaka, Japan) and irradiated under the following conditions: The laser output was in the continuous wave mode, and the emission wavelength was 10.6 μm . The maximum output power was 30 W and the beam diameter was 140 μm . The operating frequency was 24 kHz, with the duty cycle fixed at 100%. The laser spot was intentionally defocused to avoid laser ablation, while the power density was attenuated within an appropriate range by doubling the working distance between the laser output gate and target. The entire surface of the UHMWPE disk was filled with horizontal hatched lines with a nominal scan pitch of 70 μm . As a typical example of the irradiation conditions, the scan speed was set to 12,000 mm/s, with each raster line scan repeated 28 times before moving to the next pitch. The estimated energy density of the irradiation area was calculated as approximately 1.1 J/cm^2 for each scan, whereas the cumulative energy irradiated on the coated surface was approximately 31 J/cm^2 ($=1.1 \text{ J}/\text{cm}^2 \times 28$). The surface temperature of the UHMWPE disk during laser irradiation was concurrently monitored using an infrared (spectral range: 2–2.5 μm) high-speed (response time: 500 μs) digital pyrometer (IGA6/23, LumaSense Technologies, Frankfurt, Germany) at the center of the disk with a 3 mm diameter of the measurement area. Temperature calibration was performed for the coated and uncoated UHMWPE disks placed on a laboratory hot plate at various temperatures using a contact-type surface thermometer (Testo 905-T2; Testo SE & Co. KGaA, Titisee-Neustadt, Germany). The surface temperature distribution of the UHMWPE disks was measured using infrared thermography (Thermocapture THG-01; Custom Corporation, Tokyo, Japan).

2.4. Microscopy

The coating surface was observed by scanning electron microscopy (SEM) using an SU3500 (Hitachi High-Tech, Japan) equipped with an energy-dispersive X-ray spectrometer (EDS; Octane Plus, Ametek Inc. Berwyn, PA, USA) or TM4000 (Hitachi High-Tech, Osaka, Japan) with the application software of “Hitachi map 3D” for three-dimensional (3D) measurements of the surface.

2.5. Leaching of Apatite and Silica Coatings from the UHMWPE Disks

Each UHMWPE disk was coated with SrZnSiP, colloidal silica, or their mixtures, and fixed by irradiation with a CO_2 laser. The apatite coatings were selectively dissolved in dilute hydrochloric acid solution at ambient temperature. The SiO_2 coatings were dissolved in NaOH solution at ambient temperature. The samples were left overnight at ambient temperature, washed thoroughly with distilled water, and dried for microscopic observation.

2.6. Biomimetic Deposition of Calcium Phosphate from Simulated Body Fluid

Each UHMWPE disk, either coated or non-coated, was placed in a well of a 24-well cell culture plate and secured by adding 30 μL acetone. Each disk was immersed in 1 mL simulated body fluid (SBF) (Hanks' balanced salt solution, HBSS(+)). The plates were incubated at 37 $^\circ\text{C}$ in a dry oven. Each solution in the well was replaced with fresh HBSS(+) once a week during the four-week experiment. The disks were washed several times with distilled water, dried in an oven at 70 $^\circ\text{C}$, and used for SEM/EDS observations.

2.7. Determination of the Concentrations of Ions Eluted from the Coatings into Water

Each UHMWPE disk coated and irradiated was placed in a well of a 24-well cell culture plate and immersed in 1 mL of distilled water. The plates were stored in a dry oven at 37 $^\circ\text{C}$. The solution in the well was collected and refilled with fresh distilled water once a week during the four-week experiment and analyzed using inductively coupled plasma atomic emission spectroscopy (ICP-AES; Shimadzu ICPS-8100CL, Japan) to determine the concentrations of dissolved ions. The measurement for each of the sample solutions was repeated three times and the average and the standard deviation for each sample

measurement were calculated. In each case, no significant variations were found in the measured values for all samples.

3. Results

3.1. Laser Bonding of SrZnSiP on UHMWPE

Each UHMWPE disk was coated with SrZnSiP coating solution. After evaporating the ethanol solvent at ambient temperature (22–25 °C), the coated surface was irradiated using a CO₂ laser. The surface temperature was monitored using a high-speed digital pyrometer in real-time. The entire disk surface was irradiated under multiple raster scanning, with the energy density adjusted to control the maximum temperature at 150 ± 5 °C, just above the melting point of UHMWPE (140–145 °C). The melting of the surface was confirmed by observing the change in the reflection surface (from a matte to a glossy appearance). After the laser irradiation, the coated surface was rinsed in water and rubbed with a coarse paper towel. The coating surface was resistant to rubbing, and the delamination of the coating was virtually impossible, indicating that the coating layer was not only solidified by heating at an elevated temperature, but also integrated into the UHMWPE substrate. It was crucial to melt the surface of the substrate to establish an integration between the UHMWPE substrate and coatings. Applying excessive irradiation energy to the surface caused the noticeable thermal deformation or degradation of UHMWPE. The heating duration was also a crucial factor, and it was necessary to maintain the molten state for at least ten seconds to ensure tight binding over the entire surface of the disk. After several trials with systematic variations of scanning speeds and number of repetitions of raster scanning, the optimum irradiation conditions were determined as follows: the scanning speed was set to 12,000 mm/s (maximum setting), with the number of repetitions set to 28. Under these conditions, the coating was firmly fixed on the UHMWPE surface without causing any adverse effects, such as thermal deformation or the degradation of the UHMWPE substrate.

Figure 1a shows a typical temperature profile during laser irradiation under optimized conditions. The temperature measured at the center of the disk reached a maximum of 150 °C within 12 s from the start, and after passing this peak temperature, the surface temperature gradually decreased. Approximately 5 s after the completion of the irradiation, the disk surface was monitored using infrared thermography, and the results showing the temperature distribution over the disk surface are shown in Figure 1b,c. The surface temperature was flat at the center of the disk, evenly and concentrically distributed, and sharply decreased at the edge of the disk. The shape and dimensions of the disk were unaffected by laser irradiation, and the thermal energy was mainly absorbed within the coating and its boundary.

The cross-sectional analysis of the coating interface was performed. However, it could not crosscut the disk because of the typical elongation behavior of UHMWPE, even at the liquid nitrogen temperature. As an alternative, the surface of the UHMWPE disk was partially coated and irradiated using a CO₂ laser. The exposed coating edge on the disk surface was observed using a SEM equipped with 3D software. Vertical direction views are shown in Figure 2a,b, indicating that apatite coatings were built with piles of nanoparticles, with numerous nanopores on the coating surface. The approximate sizes of the apatite particles and pores were 100–300 nm and 100–200 nm, respectively. Characteristic streak patterns caused by melting were observed on the uncoated background of the UHMWPE substrate. A 3D view of the coating edge from the oblique direction is shown in Figure 2c, indicating that the apatite coatings were significantly uplifted from the substrate surfaces.

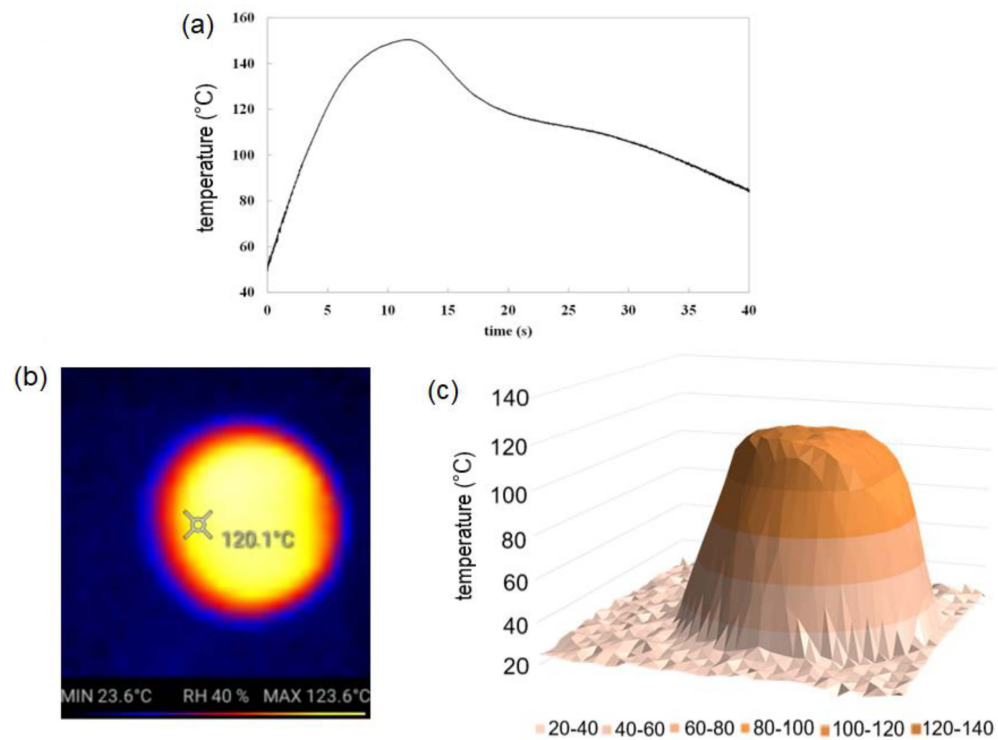


Figure 1. (a) Temperature profile of the apatite-coated UHMWPE disk during laser irradiation; (b) thermograph taken immediately after laser irradiation; and (c) graphical representation of the temperature distribution shown in (b).

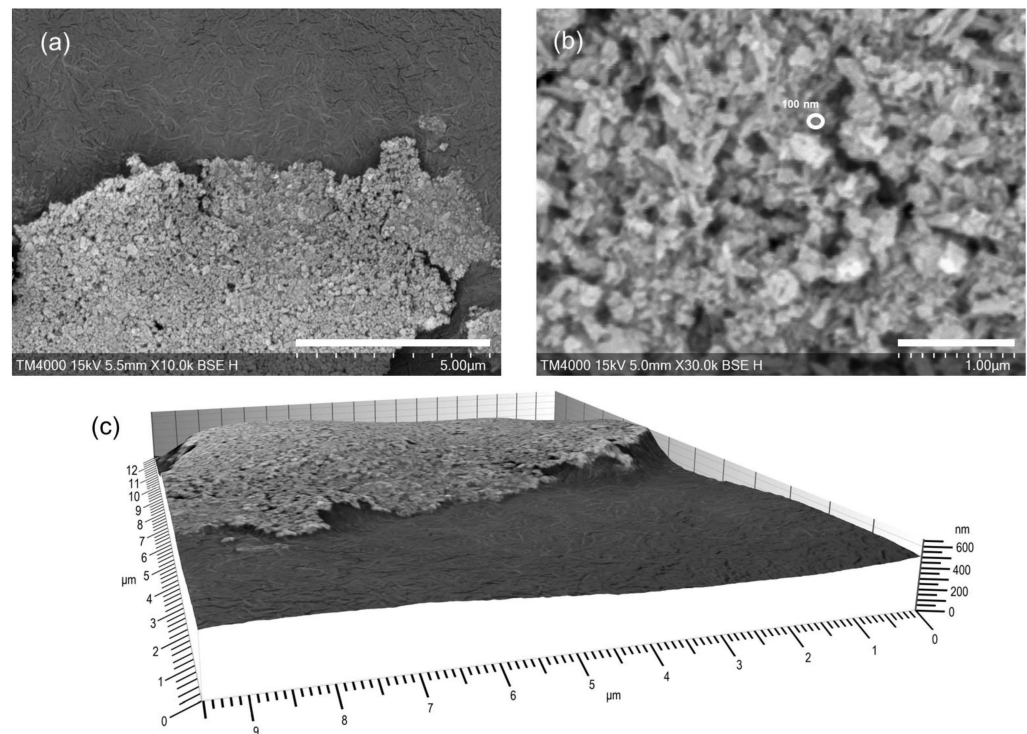


Figure 2. SEM observation of strontium apatite (SrZnSiP) coating edge after laser irradiation. (a) Magnification 10× K; (b) magnification 30× K; and (c) 3D image viewed diagonally above. Magnification 10× K.

The SEM image of the coating surface viewed at lower magnification is shown in Figure 3a. The coating surface was covered with numerous fissures caused by the volumet-

ric shrinkage of the coating mass due to the evaporation of liquid fractions in the coatings during the coating and irradiation processes. As shown in Figure 3b, the coating edge can be viewed in an oblique direction. The coating layer was uplifted by approximately $3\ \mu\text{m}$ from the substrate surface, and the noticeable subduction of the substrate surface was observed near the coating edge. Substrate uplift under the coating area appeared to be compensated by the subduction of the nearby substrate surface.

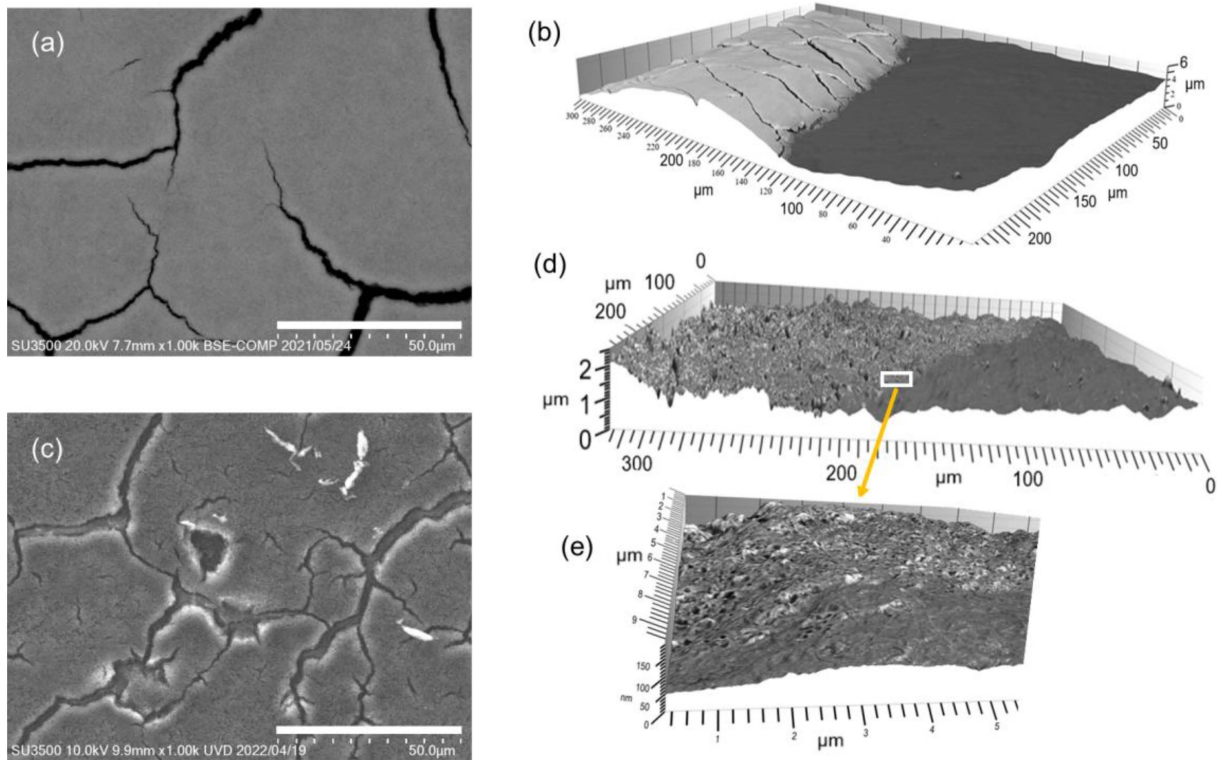


Figure 3. (a) SEM image of the SrZnSiP coating after laser irradiation. Magnification $1\times K$, and (b) 3D image of the coating edge. (c) SEM image of the acid-leached coating surface. Magnification $1\times K$, (d) 3D image of the acid-leached coating edge viewed diagonally from above. Magnification $10\times K$, and (e) enlarged view of the coating edge. Magnification $30\times K$.

The apatite particles in the coating layer were selectively dissolved in a dilute solution of hydrochloric acid at ambient temperature. The underlying substrate surface of the coated area is observed in the vertical direction, as shown in Figure 3c. The relief patterns of the apatite coatings were observed in the areas of the former apatite coatings on the substrate surface, with a significantly increased number of fissures. The crack widths observed in the original apatite coatings broadened in the relief patterns. The basal plane of the crack area appeared flat and even, whereas the substrate surface under the coated area was significantly rugged and raised upward. In the 3D image viewed from an oblique direction, as shown in Figure 3d, the precise features of this rugged surface are revealed. The expanded view of this rugged surface, as shown in Figure 3e, revealed several nanosized lumps and voids on the rugged surface. These characteristic features were considered to be the result of the capillary rise of polymer melts inside the nanopores of the apatite coatings.

3.2. Laser Bonding of Colloidal Silica on UHMWPE

A colloidal silica dispersion was coated onto the UHMWPE disks and air-dried. The coating surface was irradiated by a CO_2 laser under the same conditions as those described above. The obtained SiO_2 coatings were solidified during laser irradiation and tightly fixed to the substrate. It was impossible to delaminate the SiO_2 coatings from the UHMWPE substrate by rubbing with a coarse paper towel. The coating surface was observed using

a SEM equipped with 3D viewing software. In Figure 4a, the coating surface observed in the vertical direction is flat and featureless at this magnification. Because the average diameter of the SiO₂ particles used in this study was as small as 12 nm according to the information supplied by the manufacturer, it was impossible to distinguish each silica particle under the limited magnification of the SEM used in this study. In Figure 4b, the coating edge is observed from an oblique direction, and the interface between the SiO₂ coatings and the substrate is distinguishable by their different contrasts in the SEM images. The apparent coating thickness was 1–1.5 μm. The substrate under the SiO₂ coating was raised upward, similarly to that observed for the apatite coatings.

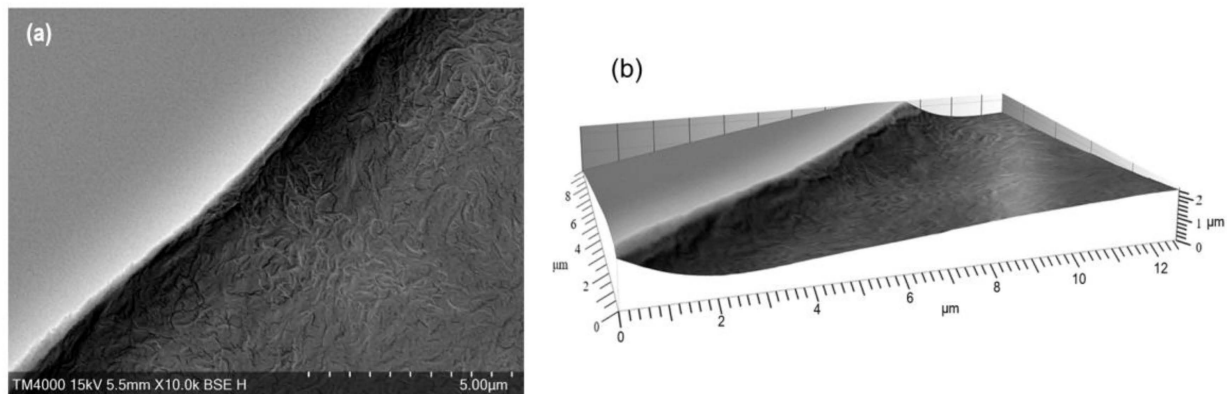


Figure 4. (a) SEM observation of the SiO₂ coating edge after laser irradiation. Magnification 10× K, and (b) 3D image of the coating edge viewed diagonally above. Magnification 10× K.

In Figure 5a, an SEM image viewed from the vertical direction at a lower magnification (1× K) is shown. The coating surface was covered with numerous cracks caused by the volumetric shrinkage of the SiO₂ coating during the coating and irradiation processes. In Figure 5b, the coating edge observed in the oblique direction shows the unique features of the steep walls of the SiO₂ coatings.

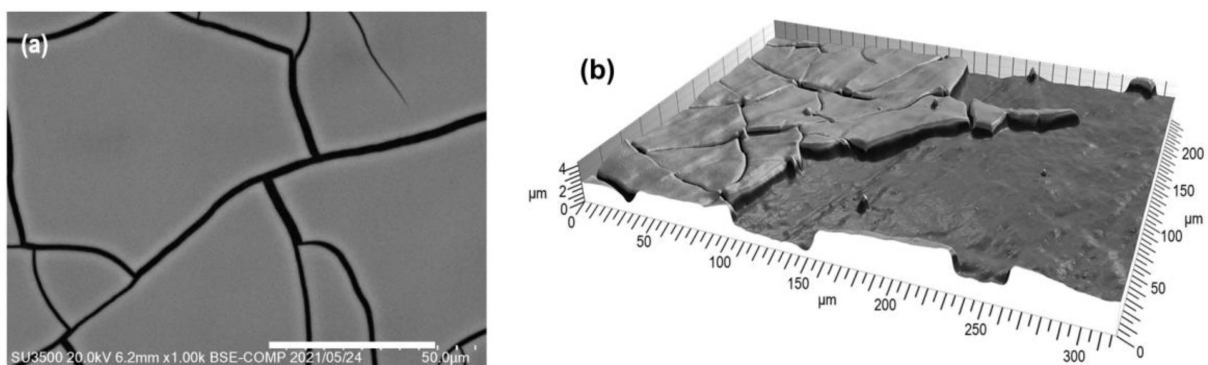


Figure 5. (a) SEM observation of the SiO₂ coating surface on UHMWPE. Magnification 1× K, and (b) 3D view of the coating edge. Magnification 1× K.

The SiO₂ layer was selectively dissolved in a dilute solution of NaOH at ambient temperature, and, as shown in Figure 6a, relief patterns of the SiO₂ coatings emerged under the formerly coated areas on the disk. The gap widths observed in the relief after the dissolution of SiO₂ were substantially broadened compared with those found in the former coatings. As shown in Figure 6b, the uplift height of the substrate is much lower than that of the former SiO₂ coatings, as shown in Figure 5b. As shown in Figure 6c, the wall of the remnant of the coating edge was examined at a higher magnification, and the uplift height was found to be approximately 250 nm. As shown in Figure 6d, the close observation of the wall face revealed parallel aligned grooves engraved on the wall of the raised surface

together with the number of nanopores associated with the grooves. These features are considered to originate from the process of polymer imbibition through the nanopores of the SiO₂ coatings.

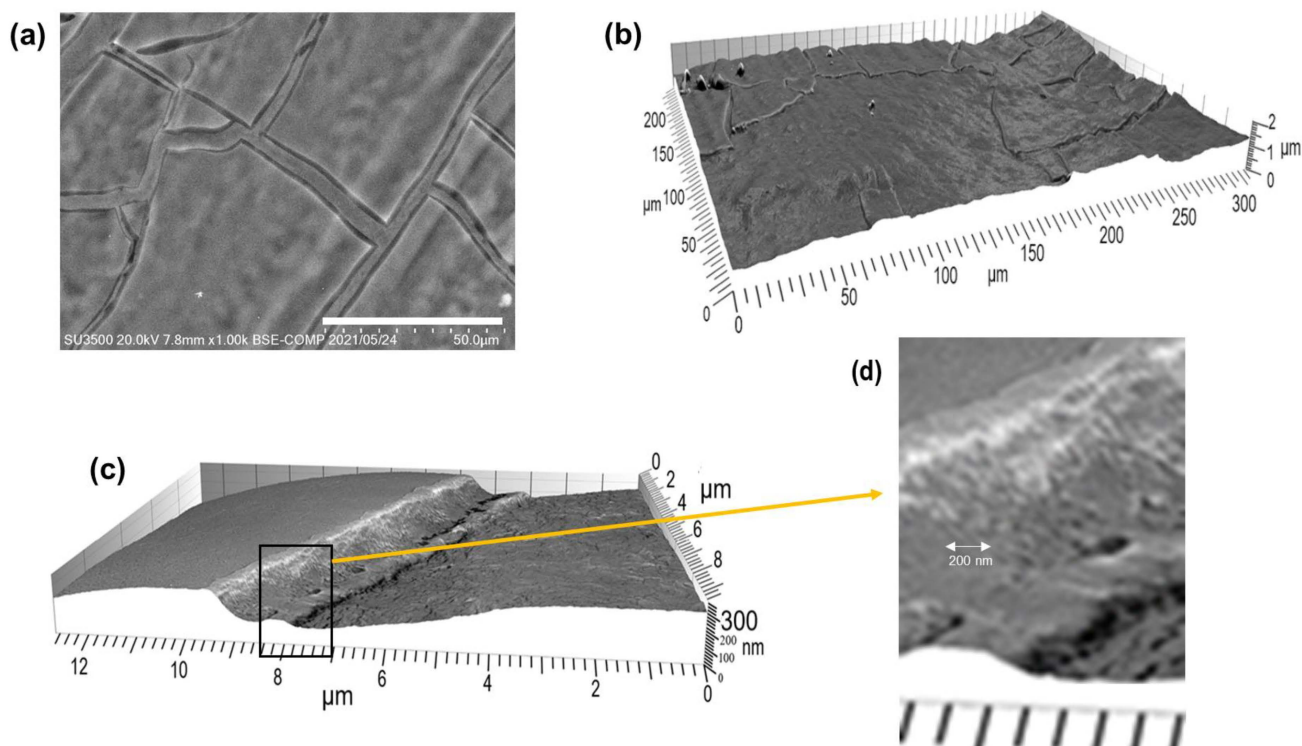


Figure 6. SEM observations of the coated area after the dissolution of SiO₂ under (a) magnification 1× K, 3D image at the edge part of coated area after leaching. (b) Magnification 1× K, (c) magnification 10× K, and (d) partially enlarged view of (c).

3.3. Laser Bonding of Binary Coatings of SrZnSiP and SiO₂ on UHMWPE

Mixed solutions of strontium apatite, SrZnSiP, and colloidal silica, SiO₂ were prepared at various weight ratios and coated onto the UHMWPE substrate, as described in Section 2.2. Each solution of the binary mixture was coated on a UHMWPE disk, air-dried, and irradiated with a CO₂ laser, as described above. In Figure 7, the SEM images of these binary coating surfaces are shown, together with those of the single coatings of SrZnSiP and SiO₂. The apatite particles, observed in Figure 7a, were easily recognized as granular small particles on the coating surface in the SEM images, whereas the SiO₂ coating, shown in Figure 7e, appeared as a featureless flat surface. In Figure 7b–d, the apatite particles seemed to be floating or embedded in the background of the SiO₂ phase, with some density fluctuations of the clusters of the apatite particles.

Further details of the features of the binary coatings were examined by elemental analyses using SEM/EDS measurements. The elemental compositions of the coating surfaces for each coating are summarized in Figure 8a–e. The peak positions of Sr and Si are situated closely nearby, their peak separations were successfully executed. As the weight ratio of SiO₂ in the coating composition increased, the observed peak intensity from Si atoms increased accordingly, and the relative intensities between the Si and Sr peaks were converted into their corresponding molar ratios. The observed Si/Sr molar ratios were plotted against the calculated values, as shown in Figure 8f, where the molecular weight of SrZnSiP was estimated to be 1449.68, from the following nominal molecular formula based on the elemental analysis; Sr₉Zn_{1.44}(PO₄)₆(SiO₄)_{1.0}(OH)_{0.0} [30]. As shown in this figure, the observed Si/Sr ratios initially increased linearly with those of the calculated values and then gradually decreased below the linear relationship at a composition of approximately

$\text{SrZnSiP}/\text{SiO}_2 = 0.25/0.75$ (Si/Sr (molar ratio) = 8.15). This observation may suggest that, at around this composition of the binary coatings, SrZnSiP particles might accumulate at the upper surface of the coating, while denser SiO_2 particles might be subducted at the bottom of the coating layer.

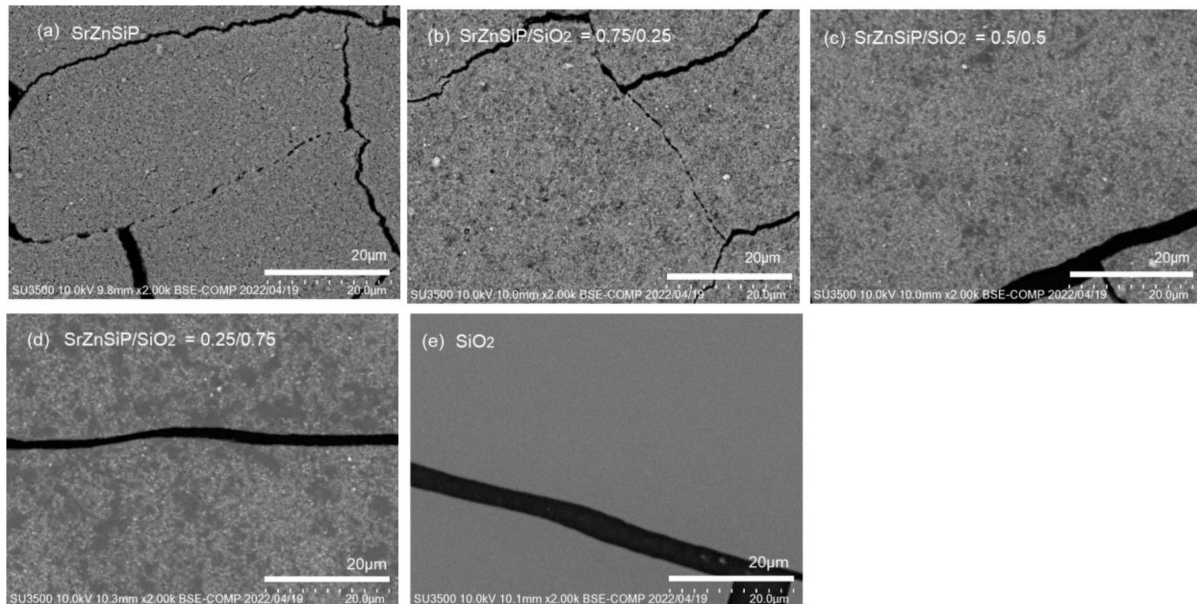


Figure 7. SEM observation of the UHMWPE disk coated by (a) SrZnSiP ; (b) mixture of SrZnSiP and SiO_2 (0.75/0.25); (c) mixture of SrZnSiP and SiO_2 (0.5/0.5); (d) mixture of SrZnSiP and SiO_2 (0.25/0.75); and (e) SiO_2 , after CO_2 laser irradiation. Magnification $2\times$ K.

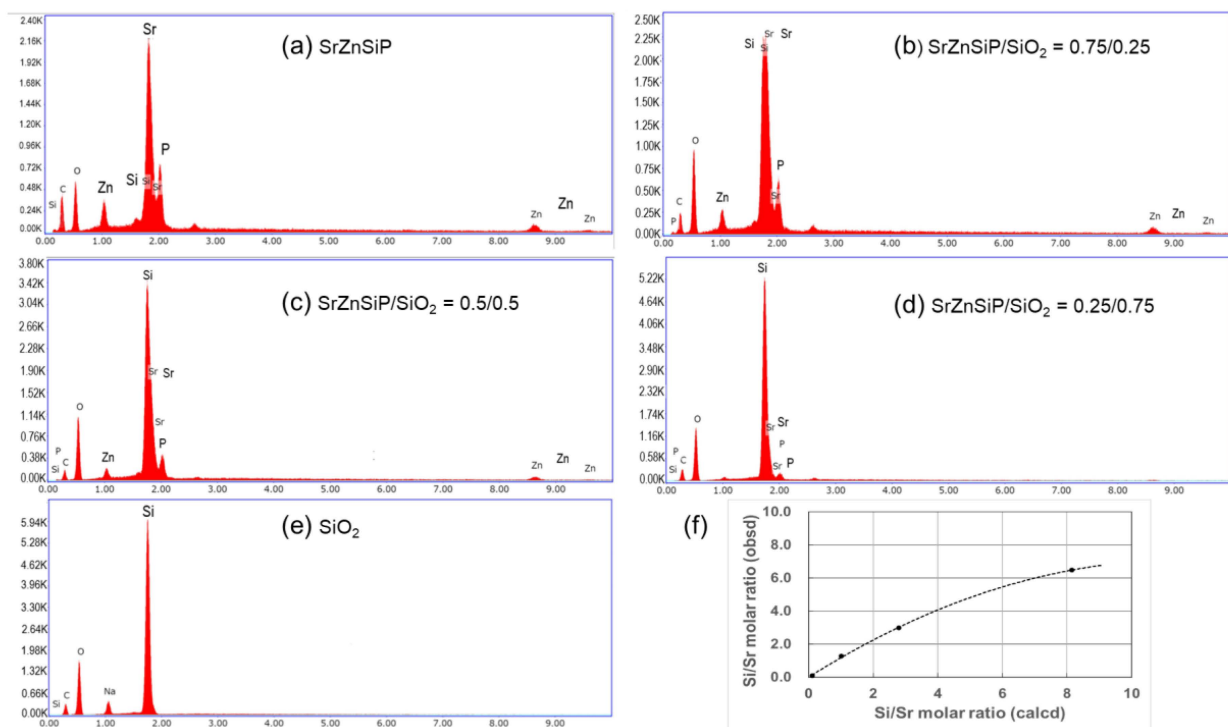


Figure 8. Elemental analyses by SEM/EDS on the coating surfaces of (a) SrZnSiP ; (b) mixture of SrZnSiP and SiO_2 (0.75/0.25); (c) mixture of SrZnSiP and SiO_2 (0.5/0.5); (d) mixture of SrZnSiP and SiO_2 (0.25/0.75); and (e) SiO_2 . (f) Plot of observed Si/Sr molar ratios shown in (a–d) vs. those of the calculated values.

The distribution of each apatite and SiO_2 phase on the coating surface was further investigated using mapping analyses in the SEM/EDS measurements. The results for the binary system of $\text{SrZnSiP}/\text{SiO}_2 = 0.25/0.75$ were shown in Figure 9. The distribution mappings for Si (Figure 9b) and Sr (Figure 9c) revealed the virtually homogeneous distributions of each element across the coating surface with some perturbation in density. The coating surface was treated with a dilute hydrochloric acid solution to selectively dissolve the apatite phase from the coating. As shown in Figure 9d,e, the SiO_2 phase emerged as a single phase with a smooth and uniform surface. The removal of the apatite particles from this binary coating did not affect the apparent features of the coating surface, which might support the speculation of the accumulation of the apatite particles on the coating surface, as mentioned above.

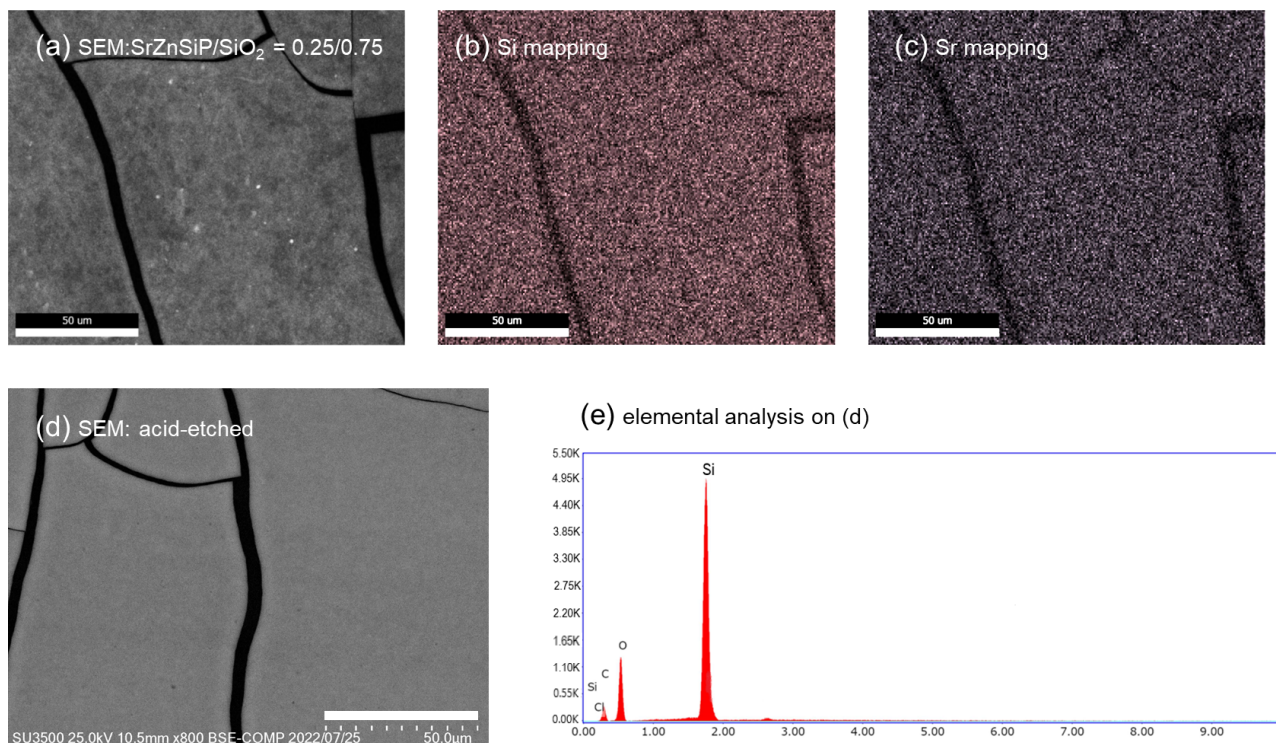


Figure 9. Mapping analyses by SEM/EDS on the coating surfaces of a mixture of SrZnSiP and SiO_2 (0.25/0.75): (a) SEM image; (b) Si mapping; (c) Sr mapping; (d) SEM image after acid treatment; and (e) elemental analysis of sample (d).

Then, the weight ratio of $\text{SrZnSiP}/\text{SiO}_2$ was increased to 0.75/0.25, and the coating surface was analyzed using SEM/EDS in the same manner. As shown in Figure 10a, the appearance of the coating changed to a roughened surface with many cracks typical of apatite coatings. As shown in Figure 10b,c, the mapping distributions of Si and Sr presented similar homogeneous distributions with a slightly noticeable perturbation in density. Figure 9d shows the rugged features of the underlying UHMWPE substrate after the selective dissolution of the apatite phase from the coating layer. In Figure 10e,f, both the mapping distribution and the intensity of Si remained unaffected by the dissolution of the apatite phase, whereas the intensity of the carbon peak from the UHMWPE substrate increased. This result suggests that the silica particles resided in a continuous phase and independently occupied the interior space in the coating layer beside the apatite particles.

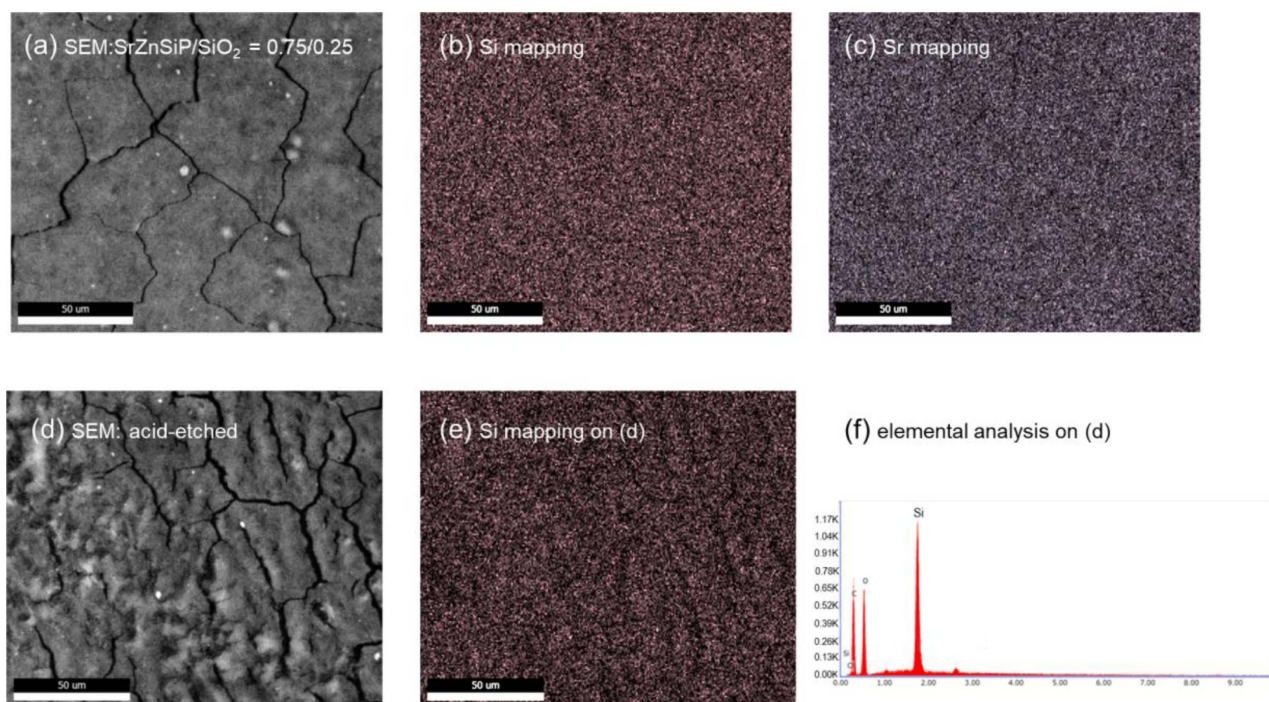


Figure 10. Mapping analyses by SEM/EDS on the coating surfaces of a mixture of SrZnSiP and SiO₂ (0.75/0.25). (a) SEM image; (b) Si mapping; (c) Sr mapping; (d) SEM image after acid treatment; (e) Si mapping of (d); and (f) elemental analysis of (d).

3.4. Biomimetic Deposition of Calcium Phosphate from Simulated Body Fluid

Each UHMWPE disk coated with either a single coat of SrZnSiP or SiO₂, or their binary mixtures, was immersed in simulated body fluid (SBF) for four weeks, and the deposition of calcium phosphate (CaP) precipitated from SBF was observed by SEM/EDS measurements. As shown in Figure 11a–e, the peak intensity from the Ca atom decreased with the increase in SiO₂ contents in the coating compositions. The relative molar ratios of precipitated CaP were evaluated using the ratio of the peak intensities of Ca/(Sr+Si). The results are shown in Figure 11f. The deposition of CaP from SBF was significantly influenced by the presence of the SiO₂ phase and the presence of the SiO₂ phase on the coating surface considerably suppressed the deposition of CaP from SBF.

The appearance of the deposited CaP phase was observed using SEM, and the images are summarized in Figure 12. On the coating surfaces, the deposition of nano-sized particles was observed and their sizes increased as the contents of SiO₂ increased. Besides these particles, the overall coating surfaces, except for SiO₂, appeared to be covered with dense layers of precipitated CaP phase, as compared with those shown in Figure 7. As shown in Figure 12e, on the SiO₂ coating, clusters of granular particles of CaP with relatively large sizes were observed, surrounded by much smaller particles in the background. Although similar particles were found on the other coating surfaces, the appearance of the deposited CaP on the SiO₂ coating suggests nucleation suppression during CaP deposition.

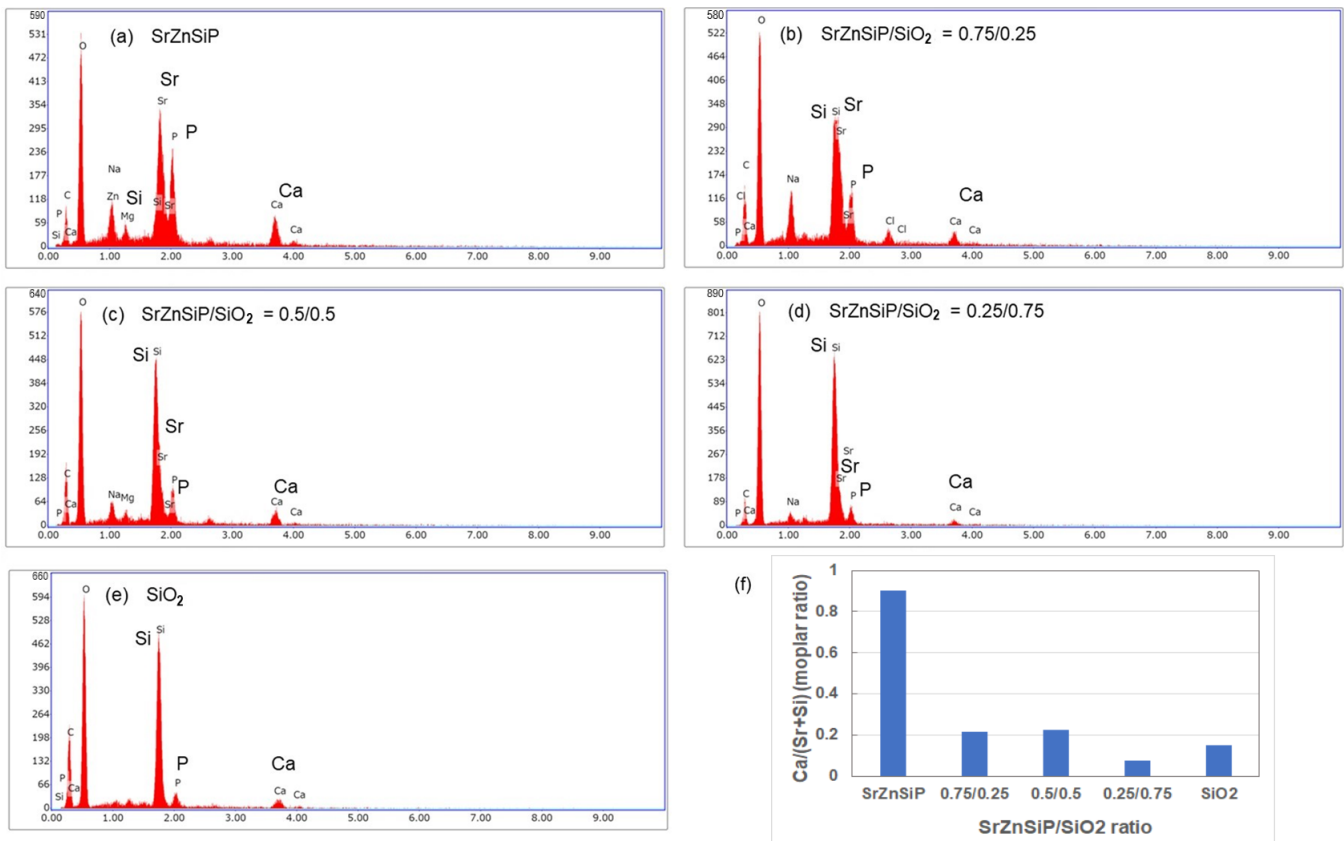


Figure 11. Elemental analyses of the coating surfaces after the biomimetic deposition of CaP by SEM/EDS. (a) SrZnSiP; (b) mixture of SrZnSiP and SiO₂ (0.75/0.25); (c) mixture of SrZnSiP and SiO₂ (0.5/0.5); (d) mixture of SrZnSiP and SiO₂ (0.25/0.75); and (e) SiO₂. (f) Plot of the observed Ca/(Si/+Sr) molar ratios shown in (a–e) for each coating.

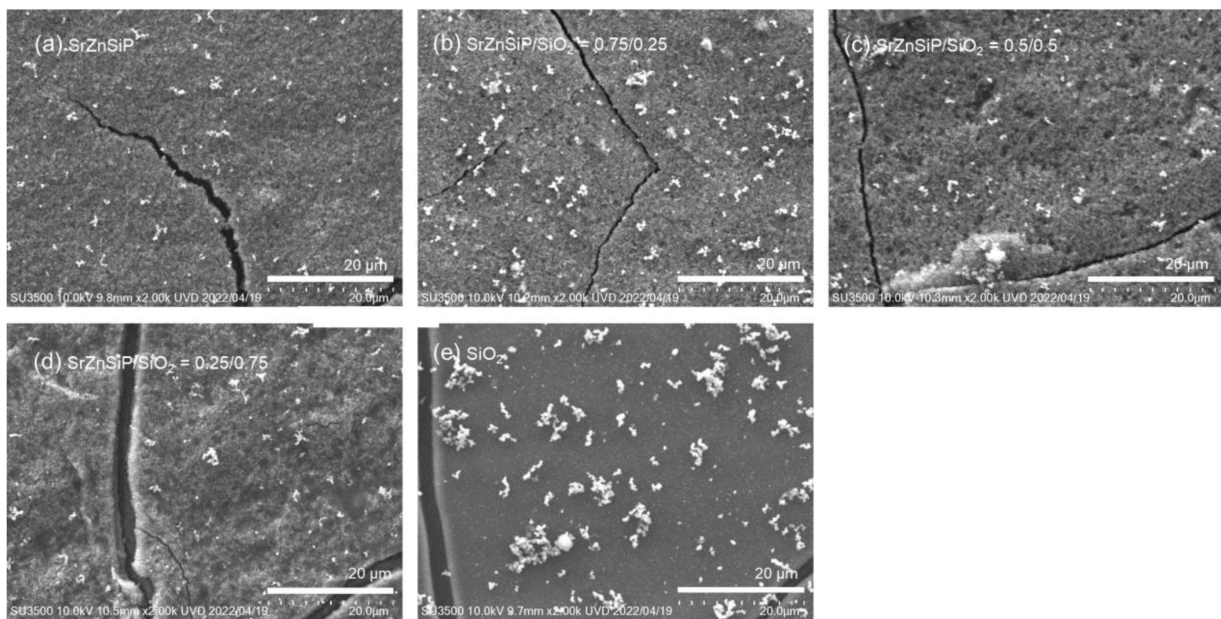


Figure 12. SEM observation of the CaP deposition on the UHMWPE disk coated with (a) SrZnSiP; (b) mixture of SrZnSiP and SiO₂ (0.75/0.25); (c) mixture of SrZnSiP and SiO₂ (0.5/0.5); (d) mixture of SrZnSiP and SiO₂ (0.25/0.75); and (e) SiO₂ after soaking in SBF. Magnification 2× K.

3.5. Dissolution Behavior of Apatite and SiO₂ Coatings

Each coated UHMWPE disk was placed in a 24-well plate, immersed in 1 mL of distilled water, and maintained at 37 °C for four weeks. Water containing eluted ions was collected and replenished with fresh water once a week until the end of the measurement. The concentrations of the various ionic species were determined using ICP-AES, and the results are summarized in Figure 13 (for the single coatings) and Figure 14 (for the binary coatings). The concentration of each ion eluted from the coatings is plotted against the immersion period. As shown in Figure 13a, the Sr and Si concentrations decreased linearly with time, whereas the Zn concentration remained virtually constant during the immersion period. This difference in dissolution behavior might reflect the different locations of these ions: Sr ions are distributed homogeneously within the apatite particles, Si ions might be localized in the external parts of the apatite particles, and Zn ions might be located in the inner parts of the particles [16]. The dissolution behavior of the SiO₂ coatings is shown in Figure 13b. The concentration of silicate ions eluted from the single SiO₂ coatings was virtually equivalent to that eluted from the inside of the apatite particles in the SrZnSiP coatings. The coatings of colloidal silica on the UHMWPE substrate formed a dense and water-resistant layer and showed negligible solubility in water, which was not suitable for our purpose of increasing the elution concentrations of silicate ions.

Then, the dissolution behavior of the binary coatings was investigated. As shown in Figure 14a–c, the concentrations of each ionic species eluted from the binary coatings composed of SrZnSiP and SiO₂ at various ratios were determined. The results indicate that the concentration of Sr ions eluted from the SrZnSiP phase was not influenced by the presence of the SiO₂ phase. As the ratio of the SrZnSiP phase decreased, the elution concentrations of Sr ions decreased proportionally. However, the concentrations of silicate ions eluted from the SiO₂ phase increased drastically as compared with those observed in the single coating, and the maximum concentrations observed in the binary coatings reached approximately 30–40 ppm, which is 5–6 times higher than those observed in the single coating. Apparently, the coexistence of apatite particles within the SiO₂ phase enhances the dissolution behavior of silicate ions from the SiO₂ phase. In all cases, during the course of the dissolution experiments, the coating surface of each sample was intact and no sign of deterioration of the coating was observed.

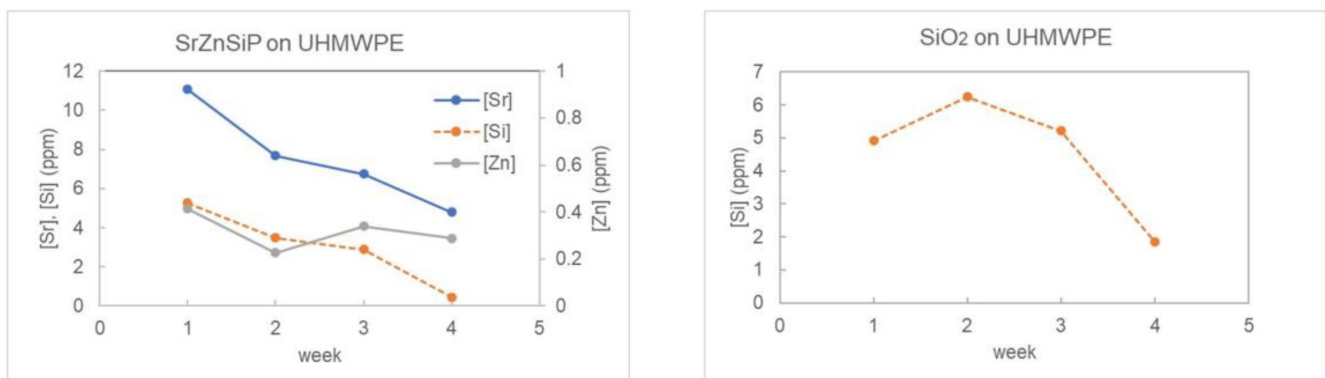


Figure 13. Variations in the concentrations of various ions released from (a) SrZnSiP coating and (b) SiO₂ coating during immersion in water for four weeks.

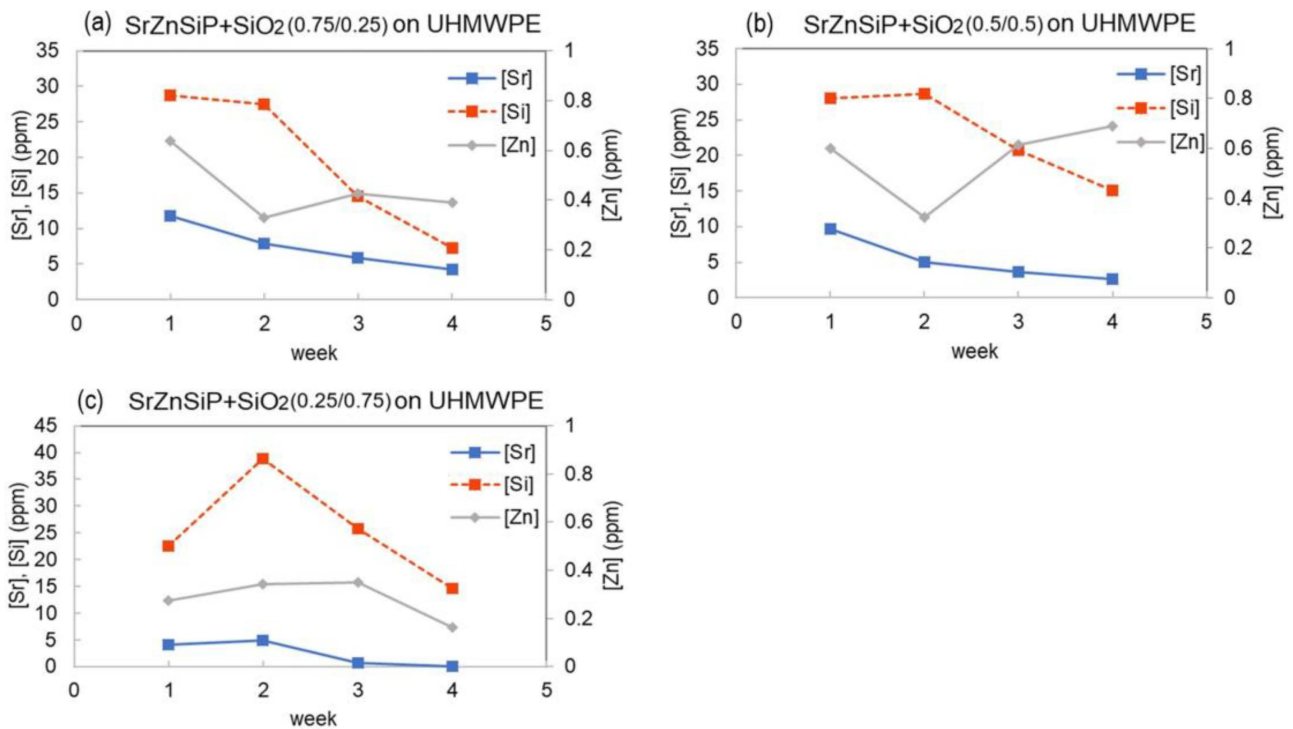


Figure 14. Comparison of dissolution behaviors of binary coatings of (a) a mixture of SrZnSiP and SiO₂ (0.75/0.25); (b) a mixture of SrZnSiP and SiO₂ (0.5/0.5); and (c) a mixture of SrZnSiP and SiO₂ (0.25/0.75) during immersion in water for four weeks.

4. Discussion

The rheological properties of UHMWPE in the molten state are characterized by its extremely high melt viscosities, owing to its extremely high molecular weight (M_w) coupled with extensive entanglements between neighboring polymer chains. Therefore, it seems improbable that the highly viscous molten UHMWPE chains could infiltrate the nanopores of the coating matrices. However, in a recent study by Resende et al. [40], they successfully demonstrated the permeation of highly viscous UHMWPE sheets inside the nanopores of anodized aluminum oxide (AAO) templates at elevated temperatures under constant pressure. They used three-dimensional AAO (3D-AAO) templates with thicknesses of 4–5 μm and interpore distances of 30 nm. Three types of polyethylene sheets—low-density, high-density, and UHMW polyethylene—were pressed on the AAO template at 170 $^{\circ}\text{C}$ for 4 h under a constant pressure of 33.7 kPa. In our study, a more efficient infiltration behavior was observed under pressure-less conditions within the order of ten seconds at approximately 150 $^{\circ}\text{C}$ and our results for this significantly enhanced infiltration behavior needs to be explained with some adequate reasoning.

The infiltration of polymer melts into porous matrices constitutes the basis of the melt infiltration technique [41], and the principle of this method is based on the capillary flow of liquid inside the pore structures. This infiltration process has been conveniently explained using a simplified classic model of a cylindrical tube into which a liquid is sucked by a capillary force. The driving force of the capillary flow is the wettability of the liquid on the wall of the capillary, while the capillary force can be expressed by the pressure difference, Δp , across the hemispherical meniscus of a liquid (with the surface tension, γ_{lv} , and the contact angle, θ) inside a cylindrical capillary of radius r_p . The classical expression of the capillary force is given by the following Laplace equation:

$$\Delta p = \frac{2\gamma_{lv} \times \cos\theta}{r_p} \quad (1)$$

In this equation, the capillary force is inversely dependent on the radius of the capillary and increases with the surface tension γ_{lv} , and the wettability of a liquid on the wall of a capillary. The critical contact angle θ_c is defined as the maximum contact angle above which the imbibition of a liquid into the capillary ceases. Therefore, the contact angle θ should be in the following range:

$$0 \leq \theta < \theta_c \text{ or } \cos\theta_c < \cos\theta \leq 1$$

The time-dependent infiltration distance, $h(t)$, of a forefront of a liquid inside a capillary can be expressed by the Lucas–Washburn equation:

$$h(t) = \sqrt{\frac{r_p \gamma_{lv} \cos\theta}{2\eta}} \sqrt{t} \quad (2)$$

where η is the melt viscosity of the liquid. By applying Equations (1) and (2), rough estimations of the capillary pressure difference Δp and the infiltration distance $h(t)$ during the laser irradiation were obtained as follows: As a typical melt viscosity of UHMWPE, the reported value of 10^7 poises = 10^6 N·s/m² for polyethylene with an M_w of 10^6 was employed [42]. Both the values of the surface free energy γ_{lv} (=0.051 N/m) and critical contact angle θ_c (=86°) for polyethylene were given by Resende et al. [27]. Assuming that the average pore radii of the apatite and SiO₂ coating layers are 10^{-7} m and 10^{-8} m, respectively, and the calculated capillary pressure difference Δp were $71 \text{ kPa} < \Delta p < 1.0 \text{ MPa}$ for the apatite coatings and $710 \text{ kPa} < \Delta p < 10 \text{ MPa}$ for the SiO₂ coatings. These values of the pressure differences were significantly larger than the applied pressure of 33.7 kPa in the experiments conducted by Resende et al. [40]. The calculated infiltration distances inside the pores of these coating layers during the irradiation period of 10 s were $42 \text{ nm} < h(10) < 160 \text{ nm}$ for the apatite coatings and $13 \text{ nm} < h(10) < 50 \text{ nm}$ for the SiO₂ coatings. The observed values of the corresponding infiltration distances were approximately 1000 nm and 250 nm, respectively, and these values are beyond the upper limits of the corresponding calculated values. It should be noted that such direct comparisons between those observed heights of polymer imbibition and the calculations based on the classical model of the capillary rise might be inappropriate, because we could not provide any evidence for the applicability of Equations (1) and (2) to the systems addressed in this study. However, the observed uplifts of the substrate were certainly the results of polymer imbibition through the void spaces within the coatings and these results may suggest a much higher mobility of polymer chains within the nanopores of the coating matrices compared to the bulk properties of polymer melts in the macroscopic dimension.

The melt flow behavior of polymers confined in nanoscale environments has been studied extensively by various researchers, and it is widely known that the macroscopic mechanism of polymer melt flow along a capillary may break down at some critical values of the diameter of the capillary. When the capillary diameter is much smaller than the dimension of polymers, the mobility of polymers becomes much higher than those found in the macroscopic bulk phase [43]. This unique non-classical behavior of polymer melts confined in nanopores has been explained using the reptation model [44,45], which described a weak molecular weight dependence of the viscosity of the polymer melt confined within a nanoscopic capillary, whose dimensions are much smaller than the radius of gyration in the bulk. According to Johner et al. [43], the dependence of the melt viscosity of a polymer on the molecular weight, M_w , transits from the classical $M_w^{3.4}$ dependency in macroscopic environments to a linear dependence on M_w within a nanoscopic capillary by passing through the boundary condition of a specific capillary diameter of 70 nm for polymers with M_w of 10^5 , with this boundary diameter found to be proportional to the molecular weight. As the molecular weight of UHMWPE used in this study was of the order of 10^6 and the pore size in the coating layer was estimated to be approximately 100 nm for the apatite coatings and approximately 10 nm for the SiO₂ coatings, a significant decrease in viscosity inside the nanopores could be expected in both cases. Interestingly, as

seen in Figures 3c and 5c, the capillary rises of polymer melts were not observed inside the relatively wide gap of the coating cracks (a few micrometers width), suggesting that the enhanced mobility of polymer melts inside the nanopores. It should be noted that the transient wetting processes of polymer melts could significantly influence the imbibition behavior [46,47] and further studies are necessary to explain the infiltration behaviors observed in this study.

The bioactivity of the surface-coated UHMWPE was evaluated using the conventional method of the biomimetic deposition of CaP in SBF. The deposition of CaP on the strontium apatite coatings was significantly suppressed by the incorporation of silica particles. According to the study by Wang et al. [48], the crystallization nucleation of hydroxyapatite in an SBF was inhibited in the presence of a relatively high concentration of silicate ions. Popa et al. [49] fabricated the bioactive-glass coatings together with varying silica contents on a titanium substrate using the magnetron sputtering deposition technique and observed the deposition behavior of CaP on them from various types of SBFs. The shapes of the deposited CaPs were found to be granular, irrespectively of the coating composition, and the amount of deposited CaP decreased as the ratio of the incorporated silica content increased. In their studies, as the concentration of the silicate ions eluted from the coatings increased, the precipitation of CaP from the SBF was suppressed, presumably owing to the influence of the formation of the relatively soluble calcium silicate complexes in the solution mixtures [50]. The results we obtained in this study agree well with those found in preceding studies.

In this study, significant enhancements in the dissolution of the SiO₂ phase were observed in the binary coatings, as compared with those in the single coatings. The incorporation of relatively large and asymmetrically shaped apatite particles into the densely packed homogeneous matrices of silica nanoparticles seems to significantly increase the apparent solubility of the silica phase. This observation might be closely related to the phenomenon of suffusion, or internal instability, which is occasionally observed in the constructs of soil or grain aggregates such as dams or levees, and this process can induce detrimental effects on the structure, leading to the erosion caused by migration and seepage of finer particles. It is widely acknowledged that the existence of the communicating void spaces within the construct structures can be susceptible to suffusion [51]. Ng et al. [52] studied the mathematical model of the binary mixtures comprising two kinds of ellipsoidal particles of different sizes. They used the discrete element method to generate numerical models of packing states using the mixtures of various ratios of these particles and exemplified a relationship between the void ratio and the composition of the particles. The minimum void ratio (or maximum packing density) was found at the critical ratio of the small particles, where the smaller particles infilled the void spaces within the primary fabric of the larger particles. Outside this critical ratio, the void spaces are partially infilled by the smaller particles and the void ratio increases. In our study, the ratios of the apatite and silica particles seem to be outside the critical value of close packing and much higher values of the void ratios could be expected, as compared with those in the case of single coatings of silica particles. In such a situation, the surface of the coating layer was exposed to the environment. Water can easily suffuse the void space, and the dissolution of silica particles proceeds efficiently. In the case of a single coating of monodispersed silica particles, sedimentation from the suspension of the coating solution might lead to closely packed dense structures of silica particles, as studied by Davis et al. [53]. In such a dense coating, the diffusion of water inside the coating layer might be suppressed and the dissolution of silica particles would be hindered. When the apatite particles were introduced to the silica coating, the close packing state of the silica particles was disturbed and excess void spaces might exist in the vicinity of the apatite particles, and the permeation of water would be enhanced at the interface between the apatite and silica particles.

This study has a limitation, which is the lack of proper statistical evaluation of some sets of results. Although all instrumental analyses carried out in this study always gave reproducible results with negligible measurement deviations, statistical analyses based on

the measurements on the plural samples prepared under the identical conditions were not carried out, due to the limitation of the maximum number of the measurable samples. Our experiments shown in this study were repeated at least twice in order to verify the validity of the results and excellent reproducibility was confirmed in every case.

As for the future perspectives, we anticipate that the present study offers a novel and promising method to establish new and future types of artificial implants which possess therapeutic functions to accelerate bone healing. It was already confirmed that various combinations of commercially available thermoplastic resins with varieties of fine ceramics could be applied for the coating processes disclosed in this paper. Aside from medical applications, broad ranges of industrial applications could be anticipated.

5. Conclusions

Surface modification of UHMWPE was performed using a newly developed laser melt infiltration technique to impart bioactivity. UHMWPE was coated with the binary mixtures of strontium apatite and colloidal silica and irradiated using a 30 W CO₂ laser to reach the maximum temperature of 150 ± 5 °C. The UHMWPE melt infiltrated the porous matrices of the coatings and formed a surface-selective composite material. The heights of capillary imbibition were evaluated by the selective dissolution of the coatings and were found to be much higher than the calculated values, suggesting a significantly lowered melt viscosity of UHMWPE inside the nanopores of the coating matrices owing to the lack of chain entanglements within a confined space. Both strontium and silicate ions are known osteo-inductive factors, with their concentrations eluted from the binary coatings determined using inductively coupled plasma atomic emission spectroscopy (ICP-AES). The concentration of eluted silicate ions drastically increased for the binary coatings owing to the increased void spaces caused by the imperfect packing of silica nanoparticles.

Author Contributions: Conceptualization, A.F. and Y.T.; methodology, A.F.; validation, A.F. and Y.T.; formal analysis, A.F.; investigation, A.F.; resources, A.F.; data curation, A.F.; writing—original draft preparation, A.F.; writing—review and editing, A.F.; visualization, A.F.; supervision, Y.T.; project administration, A.F.; funding acquisition, A.F. All authors have read and agreed to the published version of the manuscript.

Funding: This research was funded by the Amada Foundation (grant number: AF-2019217-B3).

Institutional Review Board Statement: Not applicable.

Informed Consent Statement: Not applicable.

Data Availability Statement: Not applicable.

Acknowledgments: The authors acknowledge the Nara Prefecture Institute of Industrial Development for kindly supporting this study by providing the use of LV-SEM equipped with EDS. We also express our thanks to Hitachi High-Tech, Japan, for the use of TM4000 with the application software of “Hitachi map 3D” for three-dimensional (3D) measurements.

Conflicts of Interest: The authors declare no conflict of interest.

References

1. Patil, N.A.; Njuguna, J.; Kandasubramanian, B. UHMWPE for biomedical applications: Performance; functionalization. *Polym. E* **2020**, *125*, 109529. [[CrossRef](#)]
2. Chen, J.; Gao, G.; Fu, J. Clinical Applications of UHMWPE in Joint Implants. In *UHMWPE Biomaterials for Joint Implants*; Fu, J., Jin, Z.M., Wang, J.W., Eds.; Springer: Singapore, 2019; Volume 13. [[CrossRef](#)]
3. Matsen, F.A.; Clinton, J.; Lynch, J.; Bertelsen, A.; Richardson, M.L. Glenoid component failure in total shoulder arthroplasty. *J. Bone Joint Surg. Am.* **2008**, *90*, 885–896. [[CrossRef](#)] [[PubMed](#)]
4. Strauss, E.J.; Roche, C.; Flurin, P.H.; Wright, T.; Zuckerman, J.D. The glenoid in shoulder arthroplasty. *J. Shoulder Elbow Surg.* **2009**, *18*, 819–833. [[CrossRef](#)] [[PubMed](#)]
5. Poulsson, A.H.C.; Mitchell, S.A.; Davidson, M.R.; Johnstone, A.J.; Emmison, N.; Bradley, R.H. Attachment of human primary osteoblast cells to modified polyethylene surfaces. *Langmuir* **2009**, *25*, 3718–3727. [[CrossRef](#)]

6. Nejatbakhsh, S.; Anagri, A.; Omran, A.V.; Pulpytel, J.; Bazin, C.; Ullah, M.; Mirshahi, M.; Rezaie, H.; Javadpour, J.; Khonsari, F.A. Improvement of the bioactivity of UHMWPE by two different atmospheric plasma treatments. *Plasma Chem. Plasma Proc.* **2021**, *41*, 245–264. [[CrossRef](#)]
7. Vrekhem, S.V.; Vloebergh, K.; Asadian, M.; Vercruyse, C.; Declercq, H.; Tongel, A.V.; Wilde, L.D.; Geyter, N.D.; Morent, R. Improving the surface properties of an UHMWPE shoulder implant with an atmospheric pressure plasma jet. *Sci. Rep.* **2018**, *8*, 4720. [[CrossRef](#)]
8. More, S.E.; Dave, J.R.; Makar, P.K.; Bhoraskar, S.V.; Premkumar, G.B.; Tomar, V.L. Mathe, Surface modification of UHMWPE using ECR plasma for osteoblast and osteoclast differentiation. *Appl. Surf. Sci.* **2020**, *506*, 144665. [[CrossRef](#)]
9. Reising, A.; Yao, C.; Storey, D.; Webster, T.J. Greater osteoblast long-term functions on ionic plasma deposited nanostructured orthopedic implant coatings. *J. Biomed. Mater. Res. Part A* **2007**, *1*, 78–83. [[CrossRef](#)]
10. Kurella, A.; Dahotre, N.B. Dahotre, Surface modification for bioimplants: The role of laser surface engineering. *J. Biomater. Appl.* **2005**, *20*, 5–50. [[CrossRef](#)]
11. Riveiro, A.; Maçon, A.L.; del Val, R.; Comesaña, J.; Pou, J. Laser surface texturing of polymers for biomedical applications. *Front. Phys. Sec. Optics. Photonics.* **2018**, *6*, 16. [[CrossRef](#)]
12. Neděla, O.; Slepíčka, P.; Švorčík, V. Surface modification of polymer substrates for biomedical applications. *Materials* **2017**, *10*, 1115. [[CrossRef](#)]
13. Keselowsky, B.G.; Collard, D.M.; García, A.J. Surface chemistry modulates fibronectin conformation; directs integrin binding and specificity to control cell adhesion. *J. Biomed. Mater. Res. Part A* **2003**, *66*, 247–259. [[CrossRef](#)]
14. Bacakova, L.; Filova, E.; Parizek, M.; Ruml, T.; Svorcik, V. Modulation of cell adhesion; proliferation; differentiation on materials de-signed for body implants. *Biotechnol. Adv.* **2011**, *29*, 739–767. [[CrossRef](#)]
15. Lim, J.Y.; Dreiss, A.D.; Zhou, Z.; Hansen, J.C.; Siedlecki, A.C.; Hengstebeck, R.W.; Cheng, J.; Winograd, N.; Donahue, H.J. The regulation of integrin-mediated osteoblast focal adhesion and focal adhesion kinase expression by nanoscale topography. *Biomaterials* **2007**, *28*, 1787–1797. [[CrossRef](#)]
16. Keshavarz, M.; Tan, B.; Venkatakrishnan, K. Functionalized stress component onto bio-template as a pathway of cytocompatibility. *Sci. Rep.* **2016**, *6*, 35425. [[CrossRef](#)]
17. Dadsetan, M.; Mirzadeh, H.; Sharifi-Sanjani, N.; Daliri, M. Cell behavior on laser surface-modified polyethylene terephthalate in vitro. *J. Biomed. Mater. Res.* **2001**, *57*, 183–189. [[CrossRef](#)]
18. Luo, F.; Mao, R.; Huang, Y.; Wang, L.; Lai, Y.; Zhu, X.; Fan, Y.; Wang, K.; Zhang, X. Femto-second laser optimization of PEEK: Efficient bioactivity achieved by synergistic surface chemistry and structures. *J. Mater. Chem. B* **2022**, *10*, 7014–7029. [[CrossRef](#)]
19. Torrisi, L.; Gammino, S.; Mezzasalma, A.M.; Visco, A.; Badziak, J.; Parys, P.; Wolowski, J.; Woryna, E.; Krása, J.; Láška, L.; et al. Laser ablation of UHMWPE-polyethylene by 438 nm high energy pulsed laser. *Appl. Surf. Sci.* **2004**, *1*, 164–174. [[CrossRef](#)]
20. Khalil, Y.; Hopkinson, N.; Kowalski, A.; Fairclough, J.P.A.; Materials, C.U. Characterization of UHMWPE polymer powder for laser sintering. *Materials* **2019**, *12*, 3496. [[CrossRef](#)]
21. Goodridge, R.D.; Hague, R.J.; Tuck, C.J. An empirical study into laser sintering of ultra-high molecular weight polyethylene (UHMWPE). *J. Mater. Process. Technol.* **2010**, *210*, 72–80. [[CrossRef](#)]
22. Riveiro, A.; Soto, R.; del Val, J.; Comesaña, R.; Boutinguiza, M.; Quintero, F.; Lusquiños, F.; Pou, J. Laser surface modification of ultra-high-molecular-weight polyethylene (UHMWPE) for biomedical applications. *Appl. Surf. Sci.* **2014**, *302*, 236–242. [[CrossRef](#)]
23. Macuvele, D.L.P.; Nones, J.; Matsinhe, J.V.; Lima, M.M.; Soares, C.; Fiori, M.A.; Riella, H.G. Advances in ultrahigh molecular weight polyethylene/hydroxyapatite composites for biomedical applications: A brief review. *Mater. Sci. Eng. C* **2017**, *76*, 1248–1262. [[CrossRef](#)] [[PubMed](#)]
24. Fang, L.; Leng, Y.; Gao, P. Processing of hydroxyapatite reinforced ultrahigh molecular weight polyethylene for biomedical applications. *Biomaterials* **2005**, *26*, 3471–3478. [[CrossRef](#)] [[PubMed](#)]
25. Senatov, F.S.; Kopylov, A.N.; Anisimova, N.Y.; Kiselevsky, M.V.; Maksimkin, A.V. UHMWPE-based nanocomposite as a material for damaged cartilage replacement. *Mater. Sci. Eng. C* **2015**, *48*, 566–571. [[CrossRef](#)]
26. Ortiz-Hernández, R.; Ulloa-Castillo, N.A.; Diabb-Zavala, J.M.; Estrada-De La Vega, A.; Islas-Urbano, J.; Villela-Castrejón, J.; Elías-Zúñiga, A. Advances in the Processing of UHMWPE-TiO₂ to Manufacture Medical Prostheses via SPIF. *Polymers* **2019**, *11*, 2022. [[CrossRef](#)]
27. Puértolas, J.A.; Kurtz, S.M. Evaluation of carbon nanotubes and graphene as reinforcements for UHMWPE-based composites in arthroplastic applications: A review. *J. Mech. Behav. Biomed. Mater.* **2014**, *39*, 129–145. [[CrossRef](#)]
28. Noyama, Y.; Miura, T.; Ishimoto, T.; Itaya, T.; Niinomi, M.; Nakano, T. Bone loss and reduced bone quality of the human femur after total hip arthroplasty under stress-shielding effects by titanium-based implant. *Mater. Trans.* **2012**, *53*, 565–570. [[CrossRef](#)]
29. Furukawa, A.; Kawasaki, S.; Akahane, M.; Tanaka, Y. Fabrication of bioactive poly(ether ether ketone) by laser melt infiltration of poly(ether ether ketone) inside the strontium apatite coatings. *Mater. Chem. Phys.* **2022**, *288*, 126352. [[CrossRef](#)]
30. Furukawa, A. The formation of strontium apatites through alkaline hydrolysis of strontium hydrogen phosphate and their crystallographic characterization. *Ceram. Int.* **2021**, *47*, 21848–21861. [[CrossRef](#)]
31. Egawa, T.; Inagaki, Y.; Akahane, M.; Furukawa, A.; Inoue, K.; Ogawa, M. Silicate-substituted strontium apatite nanocoating improves osteogenesis around artificial ligament. *BMC Musculoskelet. Disord.* **2019**, *20*, 396. [[CrossRef](#)]

32. Sugimoto, H.; Inagaki, Y.; Furukawa, A.; Kira, T.; Kawasaki, S.; Uchihara, Y.; Akahane, M.; Tanaka, Y. Silicate/zinc-substituted strontium apatite coating improves the osteoinductive properties of β -tricalcium phosphate bone graft substitute. *BMC Musculoskelet. Disord.* **2021**, *22*, 673. [[CrossRef](#)]
33. Kawasaki, S.; Inagaki, Y.; Akahane, M.; Furukawa, A.; Shigematsu, H.; Tanaka, Y. In vitro osteogenesis of rat bone marrow mesenchymal cells on PEEK disks with heat-fixed apatite by CO₂ laser bonding. *BMC Musculoskelet. Disord.* **2020**, *21*, 692. [[CrossRef](#)]
34. Beck, G.R.; Ha, S.-W.; Camalier, C.E.; Yamaguchi, M.; Li, Y.; Lee, J.-K.; Weitzmann, M.N. Bioactive silica-based nanoparticles stimulate bone-forming osteoblasts, suppress bone-resorbing osteoclasts, and enhance bone mineral density in vivo, Nanomedicine: Nanotechnology. *Biol. Med.* **2012**, *8*, 793–803. [[CrossRef](#)]
35. Anitha, A.; Menon, D.; Sivanarayanan, T.B.; Koyakutty, M.; Mohan, C.C.; Nair, S.V.; Nair, M.B. Bioinspired composite matrix containing hydroxyapatite-silica core-shell nanorods for bone tissue engineering. *ACS Appl. Mater. Interfaces* **2017**, *9*, 26707–26718. [[CrossRef](#)]
36. Latifi, S.M.; Fathi, M.H.; Golozar, M.A. Preparation and characterisation of bioactive hydroxyapatite–silica composite nanopowders via sol–gel method for medical applications. *Adv. Appl. Ceram.* **2011**, *110*, 8–14. [[CrossRef](#)]
37. Garibay-Alvarado, J.A.; Herrera-Ríos, E.B.; Vargas-Requena, C.L.; de Jesús Ruíz-Baltazar, Á.; Reyes-López, S.Y. Cell behavior on silica-hydroxyapatite coaxial composite. *PLoS ONE* **2021**, *16*, e0246256. [[CrossRef](#)]
38. Bogya, E.S.; Károly, Z.; Barabás, R. Atmospheric plasma sprayed silica–hydroxyapatite coatings on magnesium alloy substrates. *Ceram. Int.* **2015**, *41*, 6005–6012. [[CrossRef](#)]
39. Grandfield, K.; Zhitomirsky, I. Electrophoretic deposition of composite hydroxyapatite–silica–chitosan coatings. *Mater. Charact.* **2008**, *59*, 61–67. [[CrossRef](#)]
40. Resende, P.M.; Gutiérrez-Fernández, E.; Aguirre, M.H.; Nogales, A.; Martín-González, M. Polyethylene three-dimensional nano-networks: How lateral chains affect metamaterial formation. *Polymer* **2021**, *212*, 123145. [[CrossRef](#)]
41. de Jongh, P.E.; Eggenhuisen, T.M. Melt infiltration: An emerging technique for the preparation of novel functional nanostructured materials. *Adv. Mater.* **2013**, *25*, 6672–6690. [[CrossRef](#)]
42. Busse, W.F.; Longworth, R. Effect of molecular weight distribution and branching on the viscosity of polyethylene melts. *J. Polym. Sci.* **1962**, *58*, 49–69. [[CrossRef](#)]
43. Johner, A.; Shin, K.; Obukhov, S. Nanofluidity of a polymer melt: Breakdown of Poiseuille’s flow model. *EPL* **2010**, *91*, 38002. [[CrossRef](#)]
44. Yao, Y.; Butt, H.J.; Floudas, G.; Zhou, J.; Doi, M. Theory on capillary filling of polymer melts in nanopores. *Macromol. Rapid Commun.* **2018**, *39*, 1800087. [[CrossRef](#)] [[PubMed](#)]
45. Shin, K.; Obukhov, S.; Chen, J.T.; Huh, J.; Hwang, Y.; Mok, S.; Dobriyal, P.; Thiagarajan, P.; Russell, T.P. Enhanced mobility of confined polymers. *Nat. Mater.* **2007**, *6*, 961–965. [[CrossRef](#)]
46. Yung, K.L.; Kong, J.; Xu, Y. Studies on flow behaviors of polymer melts in nanochannels by wetting actions. *Polymer* **2007**, *48*, 7645–7652. [[CrossRef](#)]
47. Zhang, M.; Dobriyal, P.; Chen, J.-T.; Russell, T.P.; Olmo, J.; Merry, A. Wetting Transition in Cylindrical Alumina Nanopores with Polymer Melts. *Nano Lett.* **2006**, *6*, 1075–1079. [[CrossRef](#)]
48. Wang, Y.N.; Jiang, S.; Pan, H.; Tang, R. Less is more: Silicate in the crystallization of hydroxyapatite in simulated body fluids. *Cryst. Eng. Comm.* **2016**, *18*, 379–383. [[CrossRef](#)]
49. Popa, A.C.; Stan, G.E.; Husanu, M.A.; Mercioniu, I.; Santos, L.F.; Fernandes, H.R.; Ferreira, J.M.F. Bioglass implant-coating interactions in synthetic physiological fluids with varying degrees of biomimicry. *Int. J. Nanomed.* **2017**, *12*, 683. [[CrossRef](#)]
50. Chen, J.J.; Thomas, J.J.; Taylor, H.F.W.; Jennings, H.M. Solubility and structure of calcium silicate hydrate. *Cem. Concr. Res.* **2004**, *34*, 1499–1519. [[CrossRef](#)]
51. Kawano, K.; Shire, T.; O’Sullivan, C. Coupled particle-fluid simulations of the initiation of suffusion. *Soils Found.* **2018**, *58*, 972–985. [[CrossRef](#)]
52. Ng, T.T.; Zhou, W.; Ma, G.; Chang, X.L. Macroscopic and microscopic behaviors of binary mixtures of different particle shapes and particle sizes. *Int. J. Solids Struct.* **2018**, *135*, 74–84. [[CrossRef](#)]
53. Davis, K.E.; Russel, W.B.; Glantschnig, W.J. Disorder-to-order transition in settling suspensions of colloidal silica: X-ray measurements. *Science* **1989**, *245*, 507–510. [[CrossRef](#)]

Disclaimer/Publisher’s Note: The statements, opinions and data contained in all publications are solely those of the individual author(s) and contributor(s) and not of MDPI and/or the editor(s). MDPI and/or the editor(s) disclaim responsibility for any injury to people or property resulting from any ideas, methods, instructions or products referred to in the content.